

This is the accepted manuscript made available via CHORUS. The article has been published as:

# Magnetic Weyl semimetals with diamond structure realized in spinel compounds

Wei Jiang, Huaqing Huang, Feng Liu, Jian-Ping Wang, and Tony Low

Phys. Rev. B **101**, 121113 — Published 18 March 2020

DOI: [10.1103/PhysRevB.101.121113](https://doi.org/10.1103/PhysRevB.101.121113)

# Magnetic Weyl semimetals with diamond structure realized in spinel compounds

Wei Jiang,<sup>1</sup> Huaqing Huang,<sup>2</sup> Feng Liu,<sup>2</sup> Jian-Ping Wang,<sup>1</sup> and Tony Low<sup>1,\*</sup>

<sup>1</sup>*Department of Electrical & Computer Engineering,  
University of Minnesota, Minneapolis, Minnesota 55455, USA.*

<sup>2</sup>*Department of Materials Science & Engineering,  
University of Utah, Salt Lake City, UT 84112, USA*

(Dated: March 9, 2020)

We discover a  $e_g$ -orbital ( $d_{z^2}, d_{x^2-y^2}$ ) model within the diamond lattice ( $e_g$ -diamond model) that hosts novel topological states. Specifically, the  $e_g$ -diamond model yields a 3D nodal cage (3D-NC), which is characterized by a  $d$ - $d$  band inversion protected by two types of degenerate states (i.e.,  $e_g$ -orbital and diamond-sublattice degeneracies). We demonstrate materials realization of this model in the well-known spinel compounds ( $\text{AB}_2\text{X}_4$ ), where the tetrahedron-site cations (A) form the diamond sub-lattice. An ideal half metal with one metallic spin channel formed by well-isolated and half-filled  $e_g$ -diamond bands, accompanied by a large spin gap (4.36 eV) is discovered in one 4-2 spinel compound ( $\text{VMg}_2\text{O}_4$ ), which becomes a magnetic Weyl semimetal when spin-orbit coupling effect is further considered. Our discovery greatly enriches the physics of diamond structure and spinel compounds, opening a door to their application in spintronics.

Quantum topological systems have attracted tremendous attention for both exotic physics (e.g., various quantum Hall effect<sup>1,2</sup>, topological superconductivity<sup>3</sup>, Weyl fermions<sup>4</sup>) and promising applications (e.g., spintronics<sup>5</sup> and quantum computing<sup>6</sup>). In particular, Weyl semimetal systems, characterized with momentum space separated monopole pairs, Fermi arc, and the chiral anomaly, have recently been explored extensively both experimentally and theoretically<sup>7-15</sup>. **Magnetic Weyl semimetals have attracted special attention because of the intrinsic magnetic properties<sup>15-21</sup>** However, most of the studied Weyl semimetals have either both spin channels entangled near the Fermi level or Weyl points formed far away from the Fermi level<sup>13,14</sup>, adding difficulties in studying the intrinsic properties of Weyl points. It is highly desirable if the Weyl points are located at the Fermi energy, allowing topological properties to be directly explored and exploited.

Studies of two-dimensional (2D) graphene have spawned various intriguing physical phenomena<sup>22</sup>, such as Dirac fermion<sup>23</sup>, quantum Spin Hall effect<sup>1</sup>, and superconductivity<sup>24,25</sup>. It has also stimulated many branches of exciting researches, such as silicene, germanene as its 2D analogues<sup>26</sup>, valleytronics that utilize  $k$  and  $k'$  valley degree of freedom<sup>27,28</sup>, and  $p_{x,y}$ -orbital counterpart of graphene with flat band and Wigner crystallization<sup>29,30</sup>. The diamond structure, which is essentially formed by stacking buckled honeycomb layer in the A-B-C configuration, can be viewed as a three-dimensional (3D) analogue of the 2D honeycomb lattice. It is the simplest system to study analogous exotic physics in three dimensions. Based on diamond structure, theoretical proposal had indeed been made to achieve 3D topological insulators<sup>31</sup>, whose proposal has yet been able to be mapped onto real materials. It would be important to identify a physical model based on diamond structure that spawns intriguing topological states and can be realized in real materials.

One of the most famous families of materials that

hold the same group symmetry as diamond (Fd-3m) is the spinel compounds ( $\text{AB}_2\text{O}_4$ )<sup>32-34</sup>. With remarkable magnetic properties, spinel compounds have been extensively studied for decades for their promising applications, e.g, permanent magnets, power handling, and magnetic recording et al<sup>35</sup>. Surprisingly, its topological properties have been greatly overlooked<sup>12</sup>, **where only  $\text{HgCr}_2\text{Se}_4$  has been proposed to be magnetic Weyl semimetal due to the band inversion between |S> and |P> states from Se<sup>36</sup>**. Careful examinations show that there are several advantages studying topological properties of spinel compounds, including, for example, perfect diamond structure sublattice, good isolation of localized  $d$  orbitals for ideal band structure with clean topological features, versatility and high tunability, and mature materials synthesis.

Here, based on tight-binding analysis, we develop a novel two  $e_g$ -orbitals ( $d_{z^2}$  and  $d_{x^2-y^2}$ ) model on the diamond structure ( $e_g$ -diamond model). When both nearest-neighbor (NN) and next-NN (NNN) interactions are considered, the  $e_g$ -diamond bands form a Dirac/Weyl nodal cage (NC) in the 3D Brillouin zone with hourglass fermions corresponding to the Dirac/Weyl points in the 2D case. The hourglass fermions involved are protected by the coexistence of  $e_g$  orbitals degeneracy and diamond crystal symmetry with A, B sublattices degeneracy. Furthermore, we demonstrate real materials realization of the model in a representative 4-2 spinel compound ( $\text{V}^{4+}\text{Mg}_2^{2+}\text{O}_4$ ) using first-principles calculations. The spin-polarized  $e_g$ -diamond bands are exactly half-filled and isolated from other bands because of the strong tetrahedron crystal field splitting and the exchange splitting. The spin-orbit coupling effect further breaks the degeneracy of the 3D-NC, leading to the magnetic Weyl semimetal state. It is exciting to note that  $\text{VMg}_2\text{O}_4$  has excellent lattice matching (and chemical compatibility) with  $\text{MgO}$ , which is a widely used spintronics oxide material in industry. This opens the door for the realization of novel spintronics devices, such as achieving low switch-

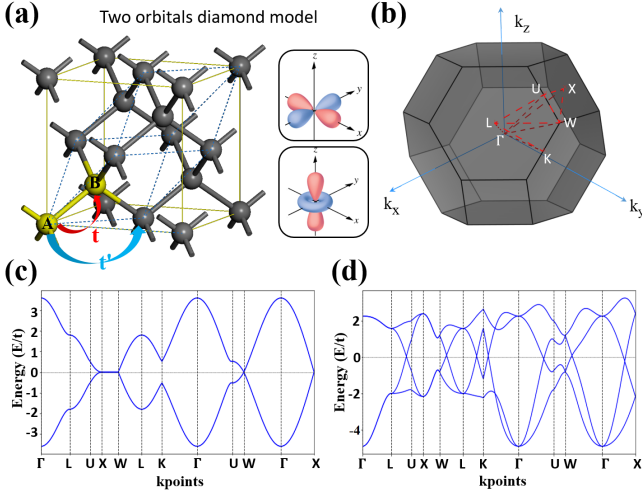


FIG. 1. **Topological semimetal in  $e_g$ -orbital diamond model.** **a** Two-orbital diamond model with nearest-neighbor  $t$  and next nearest neighbor hopping  $t'$ . Insets show the  $d_{z^2}$  and  $d_{x^2-y^2}$  orbitals for the given coordinates. **b** First-Brillouin zone with high-symmetry k-points and k-paths. **c** **Tight-binding** band structure of double degenerate single-orbital diamond model with only the NN hopping along high-symmetry paths shown in **b**. **d** **Tight-binding** band structure of  $e_g$ -diamond model with nonzero NNN hopping  $t'$ , showing various linear crossing around the Fermi level.

ing energy magnetic devices.

**Tight binding model** We first present here the 3D  $e_g$ -diamond model, different from the well-known  $sp^3$  or  $sp^3s^*$  diamond model. In the diamond structure with the face-centered cubic (FCC) Bravais lattice, there are two equivalent atomic sites in a unit cell (blue dashed lines), labelled as A and B in Fig.1a. By choosing the coordinates in Fig.1a as the orbital quantization axes, we select two energetically degenerate atomic  $d_{x^2-y^2}$  and  $d_{z^2}$  orbitals ( $e_g$  orbitals due to local tetrahedral crystal field) on each site for the  $e_g$ -diamond model. Without including the spin degree of freedom, this  $e_g$ -diamond model can be essentially described by a four-band Hamiltonian. To succinctly demonstrate the physics, we limit our Hamiltonian to only the essential NN and NNN interactions, which can be written as:

$$\mathcal{H} = \sum_i \epsilon_i d_i^\dagger d_i + \sum_{\langle i,j \rangle} t d_i^\dagger d_j + \sum_{\langle\langle i,j \rangle\rangle} t'_{ij} d_i^\dagger d_j + H.c., \quad (1)$$

where  $\epsilon_i$  represents the on-site energy of state at  $i$  site;  $d_i^\dagger$  and  $d_i$  are the creation and annihilation operators of  $d$  electrons at the site  $i$ , respectively;  $t$  and  $t'$  are the NN and NNN hoppings, respectively. In the diamond structure, each atom has four NNs and twelve NNNs. Given the strict orthogonality between the two  $e_g$  orbitals, NN hopping terms between  $d_{z^2}$  and  $d_{x^2-y^2}$  are zero. Non-zero NN hopping terms are among  $d_{z^2}$  or  $d_{x^2-y^2}$  orbitals, which have the same hopping amplitude  $t$  for  $e_g$  orbitals along four tetrahedron directions due to the geometric isotropic nature of those hoppings. More extensive TB-

model with parameters based on Slater-Koster matrix also confirms these features<sup>37</sup>.

In the absence of the NNN interactions, the same amplitude between hoppings among  $d_{z^2}$  orbitals and that among  $d_{x^2-y^2}$  orbitals guarantees the double degeneracy of the bands. This can be understood as two copies of single-orbital diamond model due to the degeneracy of two  $e_g$  orbitals on each site, as shown in Fig.1c<sup>37</sup>. In the single-orbital diamond model, the same NN hopping amplitude enables the formation of Dirac nodal lines along X-W path due to 2-fold rotation symmetries ( $C_2$  axis along x, y, and z directions through A and B sites). It is straightforward that X-W and its inversion and rotational symmetric paths (four 3-fold rotation axis along tetrahedral bond direction) will have the same degeneracy. It is important to emphasize that there exist two types of band degeneracies: type-A is due to the degeneracy of  $e_g$  orbitals ( $d_{z^2}$  and  $d_{x^2-y^2}$ ) and the type-B owing to the  $C_2$  rotational symmetry in the single-orbital diamond Hamiltonian with degenerate A and B sites.

Next, NNN hopping interactions are included. There are two types of NNN hoppings, i.e., hoppings between  $d_{z^2}$  and  $d_{x^2-y^2}$  orbitals (termed type-I thereafter,  $t'_1$ ), and hoppings among  $d_{z^2}/d_{x^2-y^2}$  orbitals (termed type-II thereafter,  $t'_2$ ). Considering each single-orbital diamond Hamiltonian as one block, type-I hopping terms mix the two unit blocks with the off-diagonal interaction, and the type-II hopping terms act as on-site energy variation of the two blocks<sup>37</sup>. Detailed analysis about effects of these two hopping terms to the band structure can be found in the supplementary materials<sup>37</sup>. Interestingly, we notice that under some symmetric hopping conditions, the band degeneracy along certain high-symmetry k-paths remains even for nonzero  $t'_1$  and  $t'_2$  NNN hoppings.

Specifically, we find that at the center of the eight hexagonal Brillouin boundary ( $K_{HC}$ ), the type-A degeneracy remains when the NNN hopping Hamiltonian keeps the  $C_4$  rotational symmetry. Similarly, at the  $\Gamma$  and any point between  $\Gamma$  and  $K_{HC}$ , the band degeneracy remains while both  $C_4$  rotational symmetry and the summation of hoppings along 12 NNN directions equals to zero<sup>37</sup>. Note the type-B degeneracy along X-W path is also conserved as the  $C_2$  rotation symmetry remains. One important outcome of the coexistence of two types of band degeneracy along different k-paths is the guaranteed band crossing (nodal point, hourglass fermion) along certain k-paths, where the two terminal k-points have different types of degeneracies, as shown in Fig. 1d. Such band crossing can be understood from the continuity nature of the wavefunctions that essentially leads to a  $d$ - $d$  band inversion, since the two degenerate bands are formed with different orbital states<sup>37</sup>. As a consequence, those nodal points surprisingly construct a three-dimensional nodal cage, which will be further discussed later.

**Magnetic semimetal in spinel compounds** To realize the aforementioned  $e_g$ -diamond model in real materials, we focus on the well-known spinel compounds that also have a space group of Fd-3m as the diamond struc-

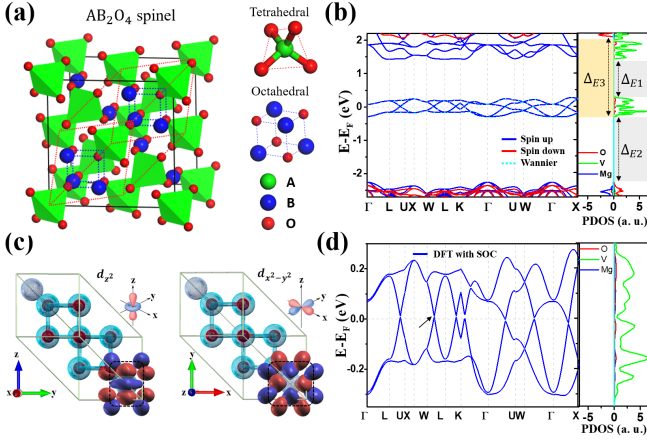


FIG. 2. **Electronic and magnetic properties of VMg<sub>2</sub>O<sub>4</sub>.** **a** Conventional atomic structure of an ionic spinel compound with chemical formula of AB<sub>2</sub>O<sub>4</sub> with the primitive unit cell labelled using dashed red lines. Cations A and B occupy the tetrahedral and octahedral sites, respectively. **b** Band structure of 4-2 spinel (V<sup>4+</sup>Mg<sup>2+</sup>O<sub>4</sub>), showing half-filled four-band structure isolated from the other bands with  $d-d$  crystal splitting gap  $\Delta_{E1}$ ,  $p-d$  charge transfer gap  $\Delta_{E2}$ , and exchange splitting gap  $\Delta_{E3}$ . Wannier fitted result is overlaid with cyan dotted lines. **c** Maximally localized wannier functions of  $d_{z^2}$  and  $d_{x^2-y^2}$  orbitals from wannier fitting. **d** Enlarged four-band structure near the Fermi level from DFT considering SOC effect. The black arrow indicates the position of Weyl points.

ture<sup>32-34</sup>. These inorganic oxides, with a chemical formula of AB<sub>2</sub>O<sub>4</sub>, are constructed by FCC lattice of O<sup>2-</sup> anions and interstitial cations in tetrahedral (T-site) and octahedral (O-site) sites formed by O<sup>2-</sup> ions, as shown in Fig.2a. It is important to mention that in normal spinels, A cations in T-sites form exactly a diamond structure and B cations in O-sites form a 3D kagome lattice instead. To the best of our knowledge, though the diamond structure made by transition metal ions exist in many compounds, their intriguing electronic and topological properties have not been studied.

For A cations, the local tetrahedral crystal field splits five degenerate  $d$  orbitals into three-fold degenerate  $t_{2g}$  and two-fold degenerate  $e_g$  orbitals. Further exchange splitting of these  $d$ -orbitals breaks the time reversal symmetry and lifts the spin degeneracy<sup>37</sup>. With proper filling of  $e_g$  orbitals, e.g., one electron per site, half-filled magnetic  $e_g$ -diamond bands can be formed around the Fermi level. Indeed, we found one experimentally studied 4-2 spinel compound (VMg<sub>2</sub>O<sub>4</sub>) that perfectly satisfies these criteria<sup>38,39</sup>, where vanadium cations ( $4s^23d^3$ ) have one  $d$  electron left after donating four valence electrons (V<sup>4+</sup>) to neighboring oxygen anions (O<sup>2-</sup>). Our density functional theory calculations<sup>37</sup> show that VMg<sub>2</sub>O<sub>4</sub> is ferromagnetic (FM) with a magnetic moment of  $2 \mu_B$  per unit cell, which are mainly contributed by V cations, as confirmed by the spin distribution plot<sup>37</sup>. The energy difference between FM and antiferromagnetic (AFM) state is

around 0.43 eV at the PBE level, indicating a promising room temperature FM feature<sup>37</sup>.

The band structure of VMg<sub>2</sub>O<sub>4</sub> without considering the spin-orbit coupling (SOC) effect is shown in Fig.2b. There is a clear spin-polarized four-band structure right at the Fermi level with very good isolation from other bands. It exhibits an ideal half-metallicity feature where one spin channel is metallic and the other spin channel is insulating with a band gap as large as 4.36 eV at the PBE level of accuracy. Further calculations using hybrid functionals show the same band structure with a even larger spin gap (5.17 eV for meta-GGA and 6.62 eV for HSE<sup>37</sup>). To understand this peculiar electronic structure, we plotted and analyzed the projected density of states (PDOS) of VMg<sub>2</sub>O<sub>4</sub>. As shown in Fig.2b, the four bands around the Fermi level are nearly half-filled and mainly contributed by V  $d$  electrons, which agrees with the magnetic moment distribution. The PDOS of Mg are located far above the Fermi level, as the two valence electrons are fully transferred to O<sup>2-</sup> ions to form the Mg<sup>2+</sup> with zero valence electrons. The oxygen states are about 2 eV below the Fermi level because of the closed shell electronic configuration.

The observed band isolation in spin up channel can be traced to the underlying energy splittings indicated as  $\Delta_{E1}$  and  $\Delta_{E2}$ , as shown in Fig.2b. The energy gap above ( $\Delta_{E1}$ ) is between  $d$  orbitals, which is essentially the tetrahedral crystal field splitting energy ( $\Delta_{tet}$ ) between  $e_g$  and  $t_{2g}$  orbitals. The large separation,  $\Delta_{tet} \approx 2$  eV, is due to strong interactions with O<sup>2-</sup> ions and the high oxidation state of V<sup>4+</sup>.  $\Delta_{E2}$  below the Fermi level is between  $d$  and  $p$  orbitals, which is the charge-transfer gap determined by the energy-level separation of orbitals between vanadium and oxygen. The separation can be well characterized by elemental electronegativity and the Madelung potential<sup>40</sup>. On the other hand, the large band gap in the spin down channel can be understood as the cooperative effect of  $\Delta_{E2}$  and  $\Delta_{E3}$ .  $\Delta_{E3}$  is essentially the exchange splitting of the V  $d$  electrons, which is known to be significant because of the strong localization effect of transition metal  $d$  orbitals. Ideally, such large gap would guarantee pure spin current and prevent any current leakage of the minority spin. To the best of our knowledge, this is also the largest spin gap among reported half-metallic ionic compounds.

**$E_g$ -diamond model and 3D-NC in VMg<sub>2</sub>O<sub>4</sub>** More interestingly, these four bands (Fig.2b) have multiple linear crossings around the Fermi level, indicating a semimetallic feature. This is also supported by the enlarged PDOS plot, which shows nearly zero DOS around the Fermi level (Fig.2d). There also exist several degenerate bands along  $\Gamma$ -L, X-W, which agree perfectly with our  $e_g$ -diamond model. To confirm the  $e_g$ -diamond model, we performed the maximally localized Wannier functions (MLWFs) calculation to fit to the DFT band structure using the Wannier90 package<sup>41</sup>. The MLWFs fitted band structure based on two  $e_g$ -orbitals on diamond lattice agrees perfectly with DFT results, as shown in Fig.2b. The calcu-



lated MLWFs show clearly the shape of  $d_{z^2}$  and  $d_{x^2-y^2}$  orbitals (Fig.2c), confirming the orbital characteristics and again validating the  $e_g$ -diamond model. This is further supported from the band-resolved partial charge distribution plot of these bands, which show a characteristic shape composed of the two orbitals<sup>37</sup>.

As demonstrated from the  $e_g$ -diamond model, we expect the band structure of  $\text{VMg}_2\text{O}_4$  to form a nodal cage in the first-Brillouin zone. To confirm the 3D-NC feature, we calculated 3D band structures in two 2D k-planes with one at the hexagonal Brillouin boundary [(111) surface, Fig.3a] and the other one at  $k_x$ - $k_y$  plane across the  $\Gamma$  point [(110) surface, Fig.3c]. The 3D band structure<sup>37</sup> and the band gap plot between middle two Dirac bands (Fig.3b and d) show clearly nodal ring features within both the hexagon (111) and octagon (110) planes. Based on the  $C_4$  rotational and the inversion symmetry, the other seven hexagonal Brillouin zone boundaries also possess the same feature as (111) surface<sup>37</sup>. Similarly, same rules apply to symmetry invariant planes of (110) surface, i.e., (101) and (011) planes across the  $\Gamma$  point due to the  $C_3$  rotational symmetry<sup>37</sup>.

From the band structure in Fig.2b, we noticed nearly all the nodal points are located closely adjacent to the Fermi level ( $< 20$  meV). Therefore, the Fermi surface could essentially capture the 3D-NC feature. Indeed, the Fermi surface plot, as shown in Fig.3e, shows a smooth surface that ends at the hexagonal Brillouin zone boundaries. Small energy dispersion of the 3D-NC lead to the coexistence of electron and hole pockets, where hole pockets are mostly located near square zone boundaries. Cross sections of the 3D Fermi/nodal cage for different planes (2D Fermi surface<sup>37</sup>) show that the nodal ring within (111) surface is nearly flat, while that of (110) surface shows small energy oscillation ( $\pm 20$  meV) as it cut across the square zone boundaries. We also calculated the 3D band structure and 2D Fermi surface for two series of 2D k-planes, i.e., (111) planes and (110) planes from the boundary to the center of the Brillouin zone, which further confirm the intriguing 3D-NC feature<sup>37</sup>.

**Magnetic Weyl semimetal** Generally, such nodal cage is not robust, which will become gapped after considering SOC effect<sup>42,43</sup>. Depending on whether the system becomes fully gapped or not, the material becomes the quantum anomalous Hall insulator or magnetic Weyl semimetal. Therefore, we proceed to include the SOC to determine the topological phases of  $\text{VMg}_2\text{O}_4$ . Firstly, we performed non-collinear calculations with different spin configurations<sup>37</sup>, which show that the system remains to be FM with nearly degenerate energies along different magnetization directions. The corresponding band structure for the magnetization direction along  $\langle 111 \rangle$  direction is plotted along high-symmetry k-paths (Fig.2d), where most of the NC become gapped with several k-points remaining degenerate, such as that along  $\Gamma$ -W that is perpendicular to the magnetic field. Detailed calculations show 18 Weyl pairs, as confirmed by the Berry phase of  $\pm\pi$  through the Berry curvature integra-

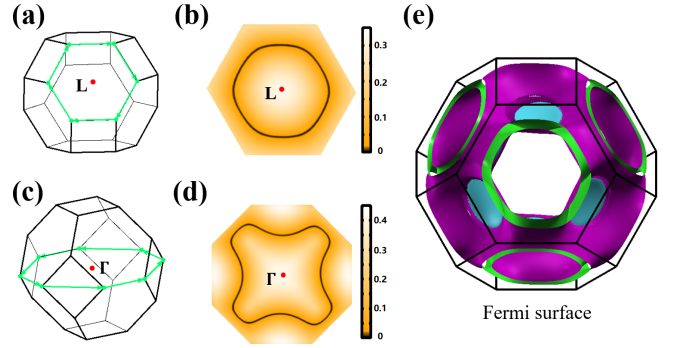


FIG. 3. **3D Nodal cage.** **a** 2D hexagonal k-plane of the (111) surface at the Brillouin zone edge. **b** Band gap between the middle two bands for the 2D k-plane in **a**. **c** and **d** same as **a** and **b** for the 2D octagonal k-plane of the (110) surface across the  $\Gamma$  point of the 3D Brillouin zone. **e** Fermi surface at the energy of Fermi level, showing the feature of 3D nodal cage. Purple and blue regions represent the hole and electron pockets, respectively. Green region highlights the cross section at the Brillouin zone boundary.

tion around these points<sup>37</sup>.

To demonstrate topological properties of  $\text{VMg}_2\text{O}_4$ , we calculated the surface state using a semi-infinite system based on Green's function. Figure 4a and d show clearly topological surface states connecting bulk states for (111) and (110) surfaces, respectively. As one of the characteristic feature of Weyl semimetals, Fermi arcs for these two surfaces are also calculated, as shown in Fig.4b and e. The Fermi arcs show dramatic difference between different surfaces due to different projections of Weyl pairs. For the (110) surface, two pairs of Weyl points can be clearly seen from the two separated Fermi arcs as required by the  $C_2$  rotational symmetry. For the (111) surface, the Fermi arcs form a “Fermi ring” with three pairs of Weyl points due to the  $C_3$  rotational symmetry. These Weyl points are accidentally overlapping while projecting to the (111) surface, which are separated within the bulk Brillouin zone. Spin textures of the Fermi arc shown in Fig.4c and f also confirm the positive and negative chirality of Weyl points.

**Discussion and perspectives** One of the intriguing properties of Weyl semimetal is their proposed large intrinsic anomalous Hall conductivity  $\sigma_H^A$ , which comes from the integration of Berry curvature from bulk band structure<sup>44,45</sup>. Considering the small charge current  $\sigma$  due to the semi-metallic feature, it is believed that Weyl semimetal could have a large anomalous Hall angle  $\sigma_H^A/\sigma$ . Therefore, we calculated intrinsic anomalous Hall conductivity of  $\text{VMg}_2\text{O}_4$ , which shows a relatively large peak ( $\approx 100 \Omega^{-1} \cdot \text{cm}^{-1}$ ) around the Fermi level<sup>37</sup>. Theoretical proposals suggest engineering extra bulk bands to cross the Fermi level may help to increase  $\sigma_H^A$ <sup>46</sup>. To test this idea, we modified the band dispersion through strain engineering and successfully realize the proposed band structure upon compressive strain. The  $\sigma_H^A$  indeed shows a large enhancement by at least 2-folds<sup>37</sup>.

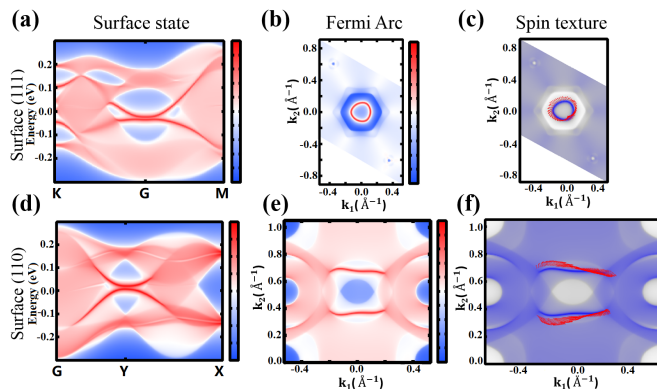


FIG. 4. **Topological properties of Weyl semimetal  $\text{VMg}_2\text{O}_4$ .** **a** Topological surface state connecting bulk states for the (111) surface. **b** and **c** Fermi arc and the corresponding spin texture of the (111) surface. **d**, **e**, and **f** Same as **a**, **b**, and **c** for (110) surface.

The intriguing phenomenon observed in  $\text{VMg}_2\text{O}_4$  can also be extended to other spinel compounds. Through theoretical calculations, we find spinel compounds formed with elements having the same valance states as  $\text{VMg}_2\text{O}_4$ , e.g.,  $\text{VMg}_2\text{Se}_4$  and  $\text{VCa}_2\text{O}_4$ , share the same features as  $\text{VMg}_2\text{O}_4$ <sup>37</sup>. On the other hand, based on the same model with different electron filling, some other potentially interesting phases can be realized with elements having different valance states. For example, we can acquire large gap ( $\approx 3$  eV) half-metal phase in  $\text{MnMg}_2\text{O}_4$  and realize an FM insulating state in  $\text{CrMg}_2\text{O}_4$ <sup>37</sup>. It is interesting to mention that FM insulator possesses two different band gaps (0.6 eV and 3.6 eV) in different spin channels, which could potentially be

used as spin filter in magnetic tunneling junction devices.

On the other hand, the lattice compatibility/match with (001) textured MgO tunneling barrier is critical for practical applications. Many materials, such as heusler materials, that have been studied face practical integration issues with MgO because of lattice mismatch. Interestingly, the material we studied here has a very small lattice mismatch with MgO for both (001) and (111) planes ( $< 0.4\%$ ), because of their structural similarity<sup>37</sup>. This lattice matching might facilitate high quality growth of  $\text{VMg}_2\text{O}_4$  directly on top of MgO to study or utilize its intriguing magnetic Weyl semimetal features. For example, we can build MTJ devices with  $\text{VMg}_2\text{O}_4/\text{MgO}/\text{VMg}_2\text{O}_4$  stacking or simply use  $\text{VMg}_2\text{O}_4$  as the spin filtering layer<sup>37</sup>.

In summary, we have discovered a novel  $e_g$ -diamond model which spawns intriguing nodal cage feature due to the coexistence of orbital and sublattice degeneracies. We discovered that such model can be realized in the well-studied spinel oxide compounds. Using 4-2 spinel compound  $\text{VMg}_2\text{O}_4$  as a representative example, we confirmed the validity of the  $e_g$ -diamond model and demonstrate the formation of 3D-NC due to linear crossing between the middle two bands. The material is calculated to be a magnetic Weyl semimetal, which is novel to spinel compounds. We further expand the model to a series of spinel compounds and demonstrate their promising applications as spintronic materials. This theoretical discovery substantially enriches the physics of spinel compounds and could potentially lead to new applications.

*Acknowledgement.* This project is supported by SMART, one of seven centers of nCORE, a Semiconductor Research Corporation program, sponsored by National Institute of Standards and Technology (NIST).

\* Corresponding author: tlow@umn.edu

- <sup>1</sup> C. L. Kane and E. J. Mele, Phys. Rev. Lett. **95**, 226801 (2005).
- <sup>2</sup> M. Z. Hasan and C. L. Kane, Rev. Mod. Phys. **82**, 3045 (2010).
- <sup>3</sup> X.-L. Qi and S.-C. Zhang, Rev. Mod. Phys. **83**, 1057 (2011).
- <sup>4</sup> B. Yan and C. Felser, Annual Review of Condensed Matter Physics **8**, 337 (2017).
- <sup>5</sup> D. Pesin and A. H. MacDonald, Nature Materials **11**, 409 (2012).
- <sup>6</sup> J. Moore, Nature Physics **5**, 378 (2009).
- <sup>7</sup> A. A. Burkov and L. Balents, Phys. Rev. Lett. **107**, 127205 (2011).
- <sup>8</sup> S.-Y. Xu, I. Belopolski, N. Alidoust, M. Neupane, G. Bian, C. Zhang, R. Sankar, G. Chang, Z. Yuan, C.-C. Lee, S.-M. Huang, H. Zheng, J. Ma, D. S. Sanchez, B. Wang, A. Bansil, F. Chou, P. P. Shibayev, H. Lin, S. Jia, and M. Z. Hasan, Science **349**, 613 (2015).
- <sup>9</sup> B. Q. Lv, H. M. Weng, B. B. Fu, X. P. Wang, H. Miao, J. Ma, P. Richard, X. C. Huang, L. X. Zhao, G. F. Chen, Z. Fang, X. Dai, T. Qian, and H. Ding, Phys. Rev. X **5**,

- 031013 (2015).
- <sup>10</sup> C. Shekhar, A. K. Nayak, Y. Sun, M. Schmidt, M. Nicklas, I. Leermakers, U. Zeitler, Y. Skourski, J. Wosnitza, Z. Liu, Y. Chen, W. Schnelle, H. Borrmann, Y. Grin, C. Felser, and B. Yan, Nature Physics **11**, 645 (2015).
- <sup>11</sup> X. Wan, A. M. Turner, A. Vishwanath, and S. Y. Savrasov, Phys. Rev. B **83**, 205101 (2011).
- <sup>12</sup> G. Xu, H. Weng, Z. Wang, X. Dai, and Z. Fang, Phys. Rev. Lett. **107**, 186806 (2011).
- <sup>13</sup> C. Felser, L. Wollmann, S. Chadov, G. H. Fecher, and S. S. P. Parkin, APL Materials **3**, 041518 (2015).
- <sup>14</sup> Z. Wang, M. G. Vergniory, S. Kushwaha, M. Hirschberger, E. V. Chulkov, A. Ernst, N. P. Ong, R. J. Cava, and B. A. Bernevig, Phys. Rev. Lett. **117**, 236401 (2016).
- <sup>15</sup> E. Liu, Y. Sun, N. Kumar, L. Muechler, A. Sun, L. Jiao, S.-Y. Yang, D. Liu, A. Liang, Q. Xu, J. Kroder, V. S. H. Borrmann, C. Shekhar, Z. Wang, C. Xi, W. Wang, W. Schnelle, S. Wirth, Y. Chen, S. T. B. Goennenwein, and C. Felser, Nature Physics **14**, 1125 (2018).
- <sup>16</sup> D. F. Liu, A. J. Liang, E. K. Liu, Q. N. Xu, Y. W. Li, C. Chen, D. Pei, W. J. Shi, S. K. Mo, P. Dudin, T. Kim, C. Cacho, G. Li, Y. Sun, L. X. Yang, Z. K. Liu, S. S. P.

- Parkin, C. Felser, and Y. L. Chen, *Science* **365**, 1282 (2019).
- <sup>17</sup> N. Morali, R. Batabyal, P. K. Nag, E. Liu, Q. Xu, Y. Sun, B. Yan, C. Felser, N. Avraham, and H. Beidenkopf, *Science* **365**, 1286 (2019).
  - <sup>18</sup> I. Belopolski, K. Manna, D. S. Sanchez, G. Chang, B. Ernst, J. Yin, S. S. Zhang, T. Cochran, N. Shumiya, H. Zheng, B. Singh, G. Bian, D. Multer, M. Litskevich, X. Zhou, S.-M. Huang, B. Wang, T.-R. Chang, S.-Y. Xu, A. Bansil, C. Felser, H. Lin, and M. Z. Hasan, *Science* **365**, 1278 (2019).
  - <sup>19</sup> S. Chowdhury, K. F. Garrity, and F. Tavazza, *npj Comput. Mater.* **5** (2019), 10.1038/s41524-019-0168-1.
  - <sup>20</sup> S. Borisenko, D. Evtushinsky, Q. Gibson, A. Yaresko, K. Koepernik, T. Kim, M. Ali, J. v. d. Brink, M. Hoesch, A. Fedorov, E. Haubold, , Y. Kushnirenko, I. Soldatov, R. Schfer, and R. J. Cava, *Nat Commun.* **10** (2019), 10.1038/s41467-019-11393-5.
  - <sup>21</sup> A. Pertsova, R. M. Geilhufe, M. Bremholm, and A. V. Balatsky, *Phys. Rev. B* **99**, 205126 (2019).
  - <sup>22</sup> A. H. Castro Neto, F. Guinea, N. M. R. Peres, K. S. Novoselov, and A. K. Geim, *Rev. Mod. Phys.* **81**, 109 (2009).
  - <sup>23</sup> K. S. Novoselov, A. K. Geim, S. V. Morozov, D. Jiang, M. I. Katsnelson, I. V. Grigorieva, S. V. Dubonos, and A. A. Firsov, *Nature* **438**, 197 (2005).
  - <sup>24</sup> B. Uchoa and A. H. Castro Neto, *Phys. Rev. Lett.* **98**, 146801 (2007).
  - <sup>25</sup> Y. Cao, V. Fatemi, S. Fang, K. Watanabe, T. Taniguchi, E. Kaxiras, and P. Jarillo-Herrero, *Nature* **556**, 43 (2018).
  - <sup>26</sup> P. Vogt, P. De Padova, C. Quaresima, J. Avila, E. Frantzeskakis, M. C. Asensio, A. Resta, B. Ealet, and G. Le Lay, *Phys. Rev. Lett.* **108**, 155501 (2012).
  - <sup>27</sup> D. Gunlycke and C. T. White, *Phys. Rev. Lett.* **106**, 136806 (2011).
  - <sup>28</sup> Y. Jiang, T. Low, K. Chang, M. I. Katsnelson, and F. Guinea, *Phys. Rev. Lett.* **110**, 046601 (2013).
  - <sup>29</sup> C. Wu, D. Bergman, L. Balents, and S. Das Sarma, *Phys. Rev. Lett.* **99**, 070401 (2007).
  - <sup>30</sup> W. Jiang, Z. Liu, J.-W. Mei, B. Cui, and F. Liu, *Nanoscale* **11**, 955 (2019).
  - <sup>31</sup> L. Fu, C. L. Kane, and E. J. Mele, *Phys. Rev. Lett.* **98**, 106803 (2007).
  - <sup>32</sup> D. S. McClure, *Journal of Physics and Chemistry of Solids* **3**, 311 (1957).
  - <sup>33</sup> P. K. Baltzer, H. W. Lehmann, and M. Robbins, *Phys. Rev. Lett.* **15**, 493 (1965).
  - <sup>34</sup> K. E. Sickafus, J. M. Wills, and N. W. Grimes, *JACS* **82**, 3279 (1999).
  - <sup>35</sup> R. Valenzuela, *Phys. Research International* **2012** (2012), 10.1155/2012/591839.
  - <sup>36</sup> J. Zou, Z. He, and G. Xu, *npj Comput. Mater.* **5** (2019), 10.1038/s41524-019-0237-5.
  - <sup>37</sup> See Supplemental Material at [URL will be inserted by publisher] for methods, tight-binding analysis, Curie temperature analysis, band formation, and non-collinear spin analysis..
  - <sup>38</sup> H. Oshima, S. Shirasaki, and H. Yamamura, *JACS* **60**, 277 (1977).
  - <sup>39</sup> J. R. Hellmann and V. S. Stubican, *JACS* **66**, 265 (1983).
  - <sup>40</sup> Y. Ohta, T. Tohyama, and S. Maekawa, *Phys. Rev. Lett.* **66**, 1228 (1991).
  - <sup>41</sup> N. Marzari and D. Vanderbilt, *Phys. Rev. B* **56**, 12847 (1997).
  - <sup>42</sup> H. Huang, W. Jiang, K.-H. Jin, and F. Liu, *Phys. Rev. B* **98**, 045131 (2018).
  - <sup>43</sup> H. Chen, S. Zhang, W. Jiang, C. Zhang, H. Guo, Z. Liu, Z. Wang, F. Liu, and X. Niu, *J. Mater. Chem. A* **6**, 11252 (2018).
  - <sup>44</sup> C. Zeng, Y. Yao, Q. Niu, and H. H. Weitering, *Phys. Rev. Lett.* **96**, 037204 (2006).
  - <sup>45</sup> S. Onoda, N. Sugimoto, and N. Nagaosa, *Phys. Rev. Lett.* **97**, 126602 (2006).
  - <sup>46</sup> E. Derunova, Y. Sun, C. Felser, S. S. P. Parkin, B. Yan, and M. N. Ali, *Science Advances* **5** (2019), 10.1126/sciadv.aav8575.